An Investigation into Methanol Oxidation Reactions and CO, OH Adsorption on Pt-Ru-Mo Catalysts for a Direct Met....

Article *in* Journal of The Electrochemical Society · February 2014

DOI: 10.1149/2.038404jes]

CITATIONS
6

READS
52

3 authors, including:

Sung-Hyeon Park
Hanyang University
19 PUBLICATIONS **244** CITATIONS
SEE PROFILE

Hak-sung Kim
Hanyang University
132 PUBLICATIONS **1,991** CITATIONS
SEE PROFILE

Journal of The Electrochemical Society, **161** (4) F405-F414 (2014)
0013-4651/2014/161(4)/F405/10/$31.00 © The Electrochemical Society

An Investigation into Methanol Oxidation Reactions and CO, OH Adsorption on Pt-Ru-Mo Catalysts for a Direct Methanol Fuel Cell

Sung-Hyeon Park,[a] Sung-Jun Joo,[a] and Hak-Sung Kim[a,b,z]

[a]*School of Mechanical Engineering, Hanyang University, Seongdong-gu, Seoul 166-791, Korea*
[b]*Institute of Nano-Science and Technology, Hanyang University, Seongdong-Gu, Seoul 133-791, Korea*

The electrochemical performance of pure Pt and Pt-based alloy nanoparticle catalysts with various Pt, Ru and Mo concentrations is investigated. Pure Pt, Ru, and Mo are first deposited on multi-walled carbon nanotubes (MWCNTs) using a E-beam evaporator (MEP5000, SNTEK), and Pt-based alloy nanoparticles are subsequently formed on the MWCNTs via flash light irradiation. Several microscopic and spectroscopic techniques, including X-ray diffractometry, scanning electron microscopy, and Raman spectroscopy are employed to characterize the catalysts. Cyclic voltammetry experiments are also performed to measure the electrochemical reactions of the Pt-based alloy nanoparticle/MWCNT catalysts. To verify the experimental results, a computational simulation analysis is conducted using molecular dynamics and the application of density functional theory. From the experimental and analytical findings, it is concluded that the Pt_{43}-Ru_{43}-Mo_{14}/MWCNT structure exhibits the best electrochemical performance for the oxidation of methanol.

Manuscript submitted September 25, 2013; revised manuscript received December 23, 2013. Published February 5, 2014.

The phenomenon of CO poisoning is a critical problem in the field of direct methanol fuel cells (DMFCs). CO poisoning occurs at pure Pt catalyst sites on the DMFC anode during the methanol oxidation reaction. The oxidation of methanol to carbon dioxide proceeds via a six-electron transfer process as follows:[1–4]

$$Pt + CH_3OH \rightarrow Pt(CO)_{ads} + 4H^+ + 4e^- \quad [1.1]$$

$$Pt + H_2O \rightarrow Pt(OH)_{ads} + H^+ + e^- \quad [1.2]$$

$$Pt(CO)_{ads} + Pt(OH)_{ads} \rightarrow CO_2 + 2Pt + H^+ + e^- \quad [1.3]$$

Strongly adsorbed CO can gradually occupy all active Pt sites according to reaction 1.1. In order to remove the $Pt(CO)_{ads}$ species, the production of $Pt(OH)_{ads}$ by reaction 1.2 is needed so that reaction 1.3 may occur. However, the formation of $Pt(OH)_{ads}$ is difficult due to its high electrochemical potential (0.7 V vs. reversible hydrogen electrode (RHE)). A promising approach to solve this issue is to form $M(OH)_{ads}$ (M = metal) species that have a low electrode potential. For example, water dissociation can occur on Ru sites with the formation of $Ru(OH)_{ads}$ species at a potential as low as 0.2 V vs. RHE.[3] Various metals (e.g., Ru, Ni, Mo, Sn, Rh, Pd) that are compatible with Pt have been proposed for the fabrication of binary, ternary, and quaternary catalysts.[5–17] In particular, Pt-Ru-Mo is considered to be one of the best Pt-based alloy catalysts.[18–21] However, the synthesis of this metal alloy is quite challenging when compared to the fabrication of pure metal nanoparticles due to the difficulty in forming a uniform material. Furthermore, controlling the concentration of each metal in the metal alloy nanoparticles is important. For example, it has been reported that excessive concentrations of Mo has a deleterious effect on methanol oxidation.[21–23]

In this study, we fabricated Pt-Ru-Mo/MWCNT catalysts with various metal atomic ratios in a short period of time (millisecond) using the flash light irradiation method under ambient conditions at room temperature.[14,15] The optimum atomic ratio of Pt, Ru, and Mo was experimentally investigated via X-ray diffractometry (XRD), scanning electron microscopy (SEM), and Raman spectroscopy. Cyclic voltammetry (CV) data were also obtained to evaluate the electrochemical performance with respect to methanol oxidation. To verify the experimental results, we conducted a computational simulation analysis using molecular dynamics (MD) and the application of density functional theory (DFT). The analytical results were ultimately compared to the experimental findings.

[z]E-mail: kima@hanyang.ac.kr

Experiments

Material preparation.— Pt-based alloy nanoparticle/MWCNT composite catalysts were prepared as follows. First, 8 mg of MWCNTs (CM-95, > 99% purity, diameter 10 ∼ 15 nm, length 200 μm, Hanwha Nano Technology) and 45 mL of N-dimethylformamide (DMF) (99.8%, Sigma-Aldrich Co.) were mixed together in an ultrasonic bath for 2 h. The resulting MWCNT/DMF solution was then spread on a silicon wafer and dried at 120°C on a hot plate. An electron beam evaporator (MEP5000, SNTEK) was employed to deposit metal layers onto the MWCNTs (total mass of metals = 2 mg); the purity of all metals was greater than 99.99%. The different Pt-based catalyst compositions investigated in this study are denoted as:

Pt_{100}/MWCNT (Case 1), Pt_{50}-Ru_{50}/MWCNT (Case 2), Pt_{43}-Ru_{43}-Mo_{14}/MWCNT (Case 3), Pt_{50}-$Ru_{37.5}$-$Mo_{12.5}$/MWCNT (Case 4), Pt_{50}-Ru_{25}-Mo_{25}/MWCNT (Case 5), Pt_{50}-$Ru_{12.5}$-$Mo_{37.5}$ /MWCNT (Case 6).

To form Pt-alloy nanoparticles on the MWCNTs, the metal-coated MWCNTs were subjected to flash light irradiation (Fig. 1a). The light source was a xenon lamp that emitted a spectrum of light covering a wide range of wavelengths from 380 nm to 1.0 μm through arc plasma generation (Fig. 1b).[19] In our previous work, the pulse number, width, and gap were optimized at 3 times, 5 ms, and 5 ms, respectively, and a total pulse energy of 60 J/cm^2 was chosen to form uniform and well dispersed Pt-alloy nanoparticles on the MWCNTs.[19] After flash light irradiation, the Pt-alloy nanoparticle/MWCNT catalysts were mixed with 3.5 mL of ethanol (> 99.9% purity, Samchun. Co) and 0.7 mL of a 5 wt% Nafion solution (MW = 1100, perfluorinated ion exchange resin, 5 wt% solution, DuPont Co.). The resulting solution was stirred for 1 h using an ultrasonicator.

Characterization.— To characterize the particle size and phase of the materials, crystal phase analysis was conducted using XRD (D/MAX RINT 2000**,** Rigaku, CuKα radiation). The morphology of the Pt-based alloy nanoparticle catalysts was examined by SEM (S4800, Hitachi, 15 kV operating voltage).

To characterize the electrochemical activities of the catalysts with respect to methanol oxidation, CV tests were performed using a potential stat (CompactStat, Ivium Technologies) with a three-electrode cell in a 0.5 M H_2SO_4 + 1 M CH_3OH solution. All CV experiments were conducted at room temperature at a scan rate of 50 mV/s from −0.3 V to 1.0 V (vs. Ag/AgCl); each sample was scanned five times.[19] A glassy carbon electrode (GCE, I.D 3 mm, O.D 6 mm, CHI Co.) was polished to a mirror finish with 0.05 μm alumina. Five microliters of the catalyst slurries and 5 μL of a 5 wt% Nafion solution were then loaded onto the surface of the electrode. For catalyst loading, the GCE was dried at 70°C using a heat gun. A Ag/AgCl electrode (CHI Co.)

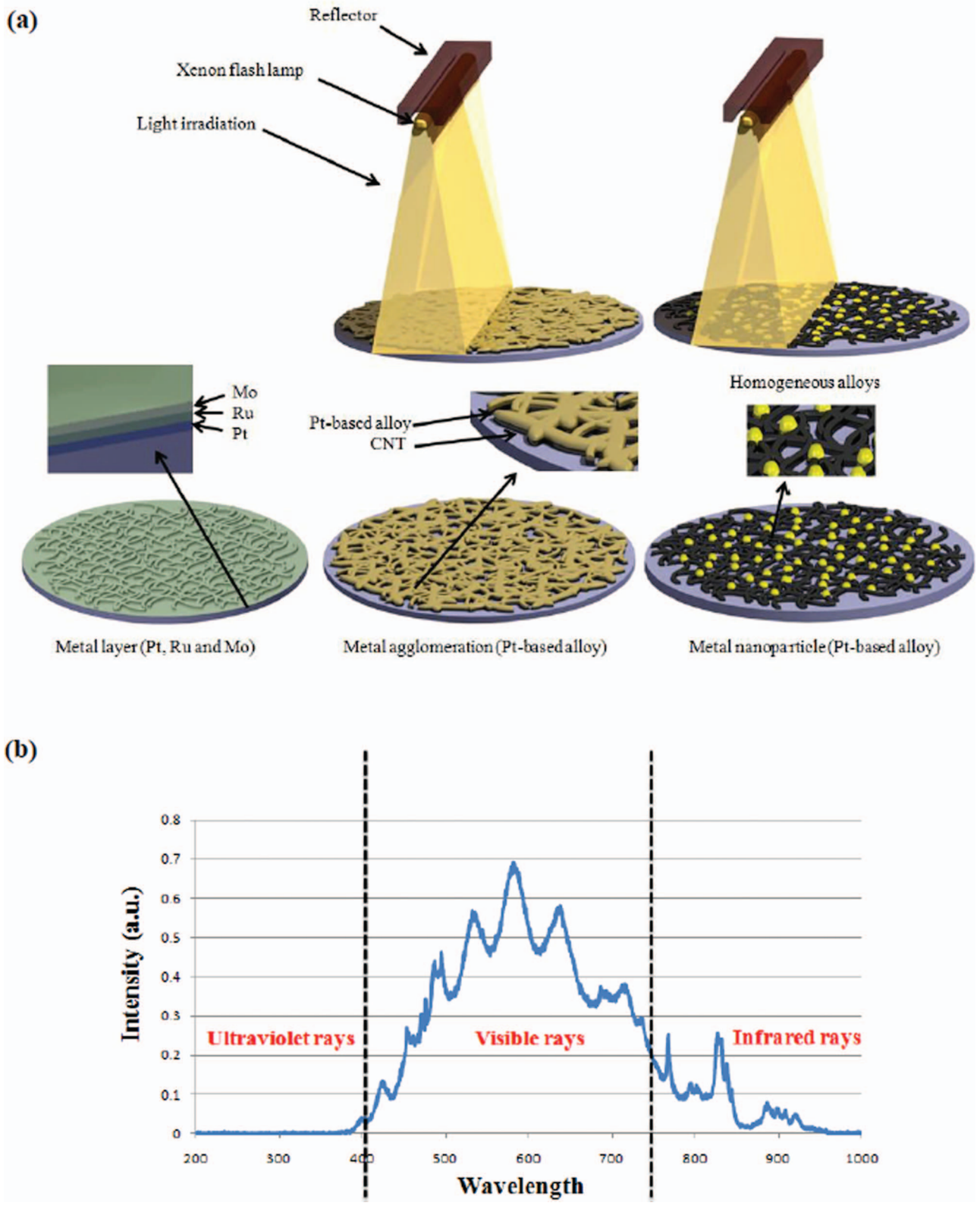

Figure 1. (a) The schematic of process for synthesizing metal alloys using flash light irradiation and (b) wavelength spectra of the flash light.

saturated in 3.3 M KCl and a Pt wire were used as the reference and counter electrodes, respectively.

Molecular dynamics study.— To verify the experimental results, computational simulation analysis was carried out using MD. Here, DFT was employed to calculate the CO and OH adsorption energies on both Pt_{100} and Pt_{50}-Ru_{50} surfaces, as well as on Pt-Ru-Mo trimetallic surfaces with various metal concentrations. Periodic slab calculations were performed using the Cambridge Serial Total Energy Package (CASTEP), which exhibits excellent performance in the

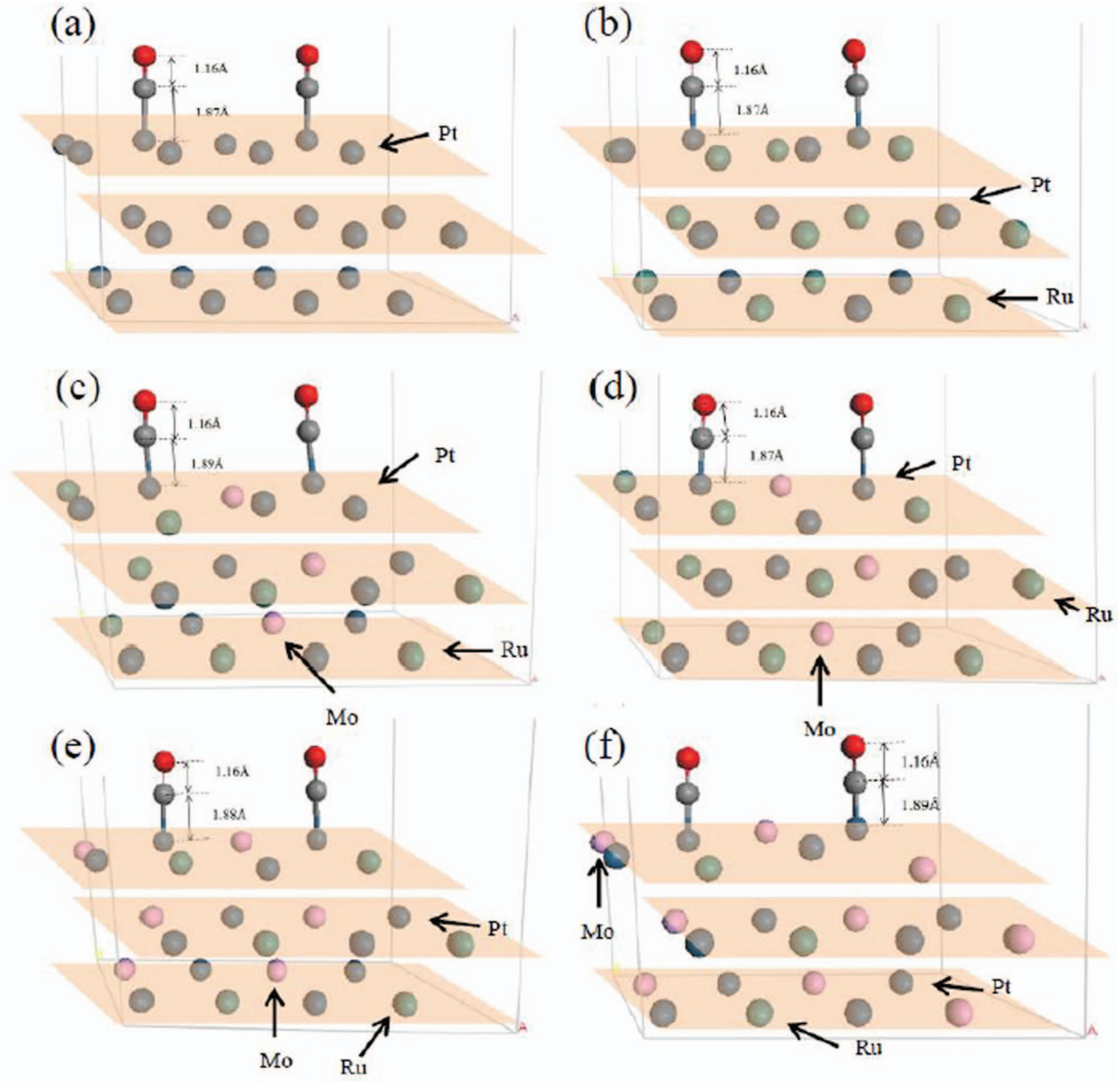

Figure 2. The image of CO molecule adsorbed on the atop sites with various surfaces : (a) Pt_{100}, (b) Pt_{50}-Ru_{50} (c) Pt_{43}-Ru_{43}-Mo_{14}, (d) Pt_{50}-$Ru_{37.5}$-$Mo_{12.5}$, (e) Pt_{50}-Ru_{25}-Mo_{25}, (f) Pt_{50}-$Ru_{12.5}$ -$Mo_{37.5}$ cases.

analysis of metallic surfaces.[24–26] The Kohn-Sham equations were utilized to solve the DFT-Generalized Gradient Approximation (GGA), while ultrasoft pseudopotentials were used to describe the ionic cores.[27] The plane wave cutoff energy of 400 eV was used in the calculation of the compact convergence for systems. Also, a Monkhorst-Pack scheme k-point mesh with a size of 2 × 4 × 1 was employed for sampling the Brillouin zone.[28,29] No spin polarization or density-mixing scheme was used in the simulations.

Based on the platinum face-centered cubic (fcc) bulk structure. Four-atomic layered Pt (111) surface model was built with coverage of adsorbates of 0.25 ML for the relaxed condition.[29] All Pt-based alloy catalysts were modeled as 4 × unit cells using the supercell approach, as shown in Fig. 2 and Fig. 3. A 15 Å vacuum separated the top and bottom of the slabs along the surface direction. The reaction leading to CO removal occurs based on CO and OH adsorption on the metal alloy surfaces as follows:[2]

$$M(CO)_{ads} + M(OH)_{ads} \rightarrow 2M + (CO)_2(g) + H^+ + e^- \qquad [2.1]$$

The affinity of the above CO removal reactions with respect to the compositions of the metal alloys can be calculated according to the electrochemical potential of the CO and OH adsorption reaction on the surfaces of the metals. The adsorption energies of CO and OH molecules on the metals can be calculated as follows:

$$\Delta E_{ad\_CO} = E_{M-CO} - E_{layer} - E_{CO\,molecule} \qquad [2.2]$$

$$\Delta E_{ad\_OH} = E_{M-OH} - E_{layer} - E_{OH\,molecule} \qquad [2.3]$$

It was assumed that CO and OH molecules are placed on all metal sites and all forms of adsorbed CO and OH were situated atop a layer of the metal in the (111) direction.[3,29–38] The convergence criteria for energy calculation and structure optimization were set as 2.0 × 10^{-5} eV/atom, 2.0 × 10^{-6} eV/atom, 0.05 eV/ Å and 2.0 × 10^{-3} Å for the tolerance of energy, self-consistent field, maximum force, and maximum displacement, respectively. These parameters were used for the carbon monoxide case and hydroxyl case (Fig. 3).

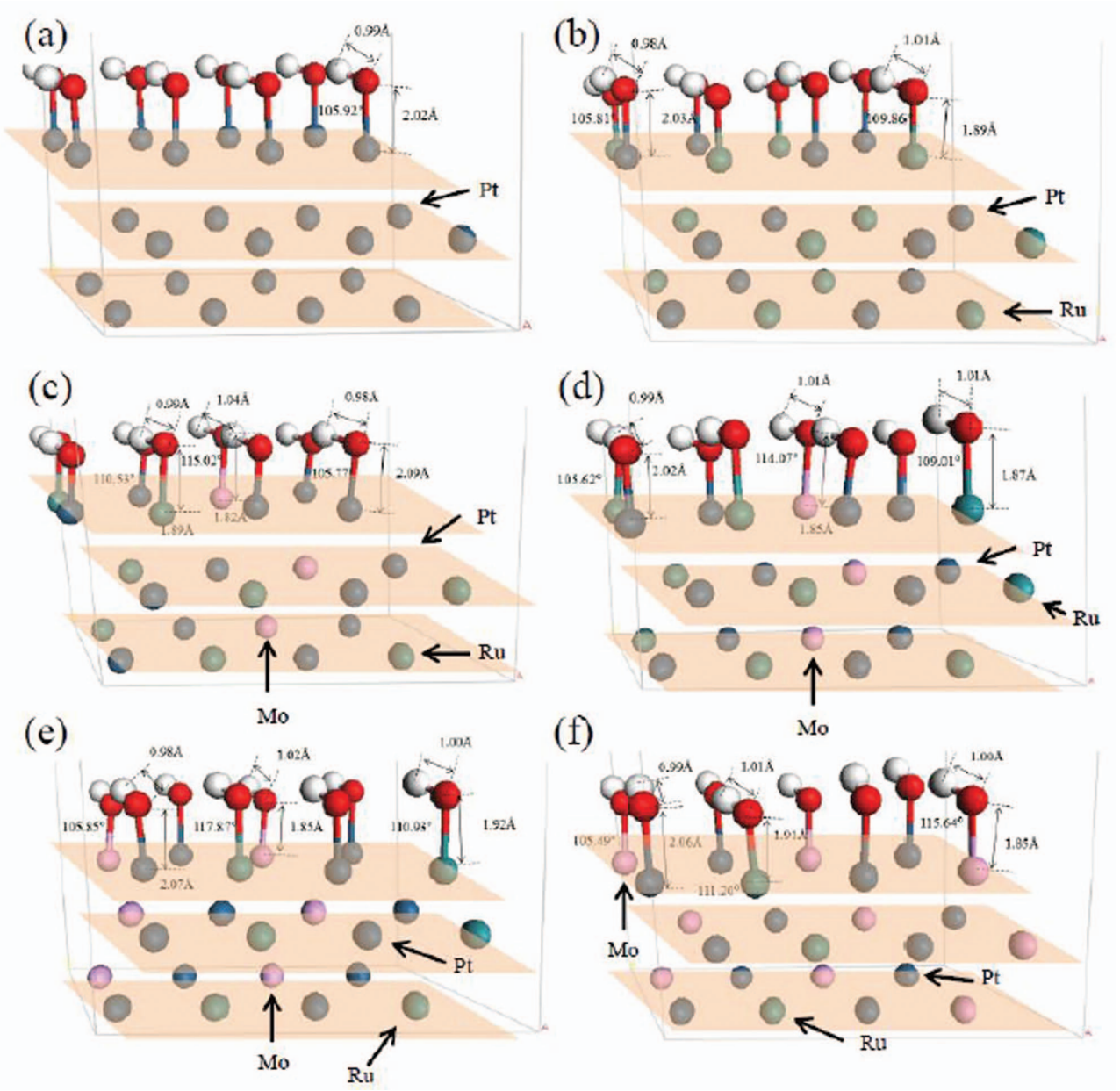

Figure 3. The image of OH molecule adsorbed on the atop sites with various surfaces : (a) Pt_{100}, (b) Pt_{50}-Ru_{50} (c) Pt_{43}-Ru_{43}-Mo_{14}, (d) Pt_{50}-$Ru_{37.5}$-$Mo_{12.5}$, (e) Pt_{50}-Ru_{25}-Mo_{25}, (f) Pt_{50}-$Ru_{12.5}$-$Mo_{37.5}$ cases.

Results and Discussion

Experimental results.— SEM images were obtained to evaluate the formation of the Pt-based alloy catalysts with respect to the flash light energy; the results are shown in Fig. 4. In our previous paper, deposited Pt, Ru, and Mo layers on MWCNTs began to melt and agglomerate when the light energy was greater than 40 J/cm^2, while metal nanoparticle-alloys were completely formed when the light energy was 60 J/cm^2.[19] Therefore, a flash light energy of 60 J/cm^2 was applied to all specimens for the formation of metal nanoparticle-alloys with a nanoscale "bumpy" structure. As shown in Fig. 4, the metal nanoparticle-alloys were well-dispersed on the MWCNTs. In all cases, a morphology consisting of larger (∼100 nm diameter) Pt-alloy nanoparticles and smaller (∼5 nm) nanoparticles was observed. The formation of smaller (∼5 nm) size nanoparticles would be beneficial to electrochemical performance, as it serves to increase the reaction surface area of the catalyst. A possible mechanism for the formation of irregular-shaped smaller nanoparticles could be the agglomeration and solidification of molten metal produced by flash light irradiation at structural imperfections (e.g., defects, misalignment regions, and impurities) on the MWCNTs during the formation of the nanoscale "bumpy" structure (Fig. 5).

The XRD patterns of the Pt-based alloy nanoparticle/MWCNT catalysts prepared by flash light irradiation are shown in Fig. 6. The Pt, Ru, and Mo metal alloys yielded diffraction peaks corresponding to (111), (220), and (311) planes at 2θ values of 39.8°, 67.4°, and 81.9°, respectively, while a (100) peak at a 2θ value of 42.4° was produced by graphite in the MWCNTs. Compared to the diffraction peaks of pure platinum, those of the Pt-Ru and Pt-Ru-Mo alloys were shifted to higher 2θ values as the atomic ratios of Ru and Mo were increased; no peaks corresponding to pure ruthenium or molybdenum were observed. The obtained XRD results provide clear evidence of homogeneous alloy nanoparticle formation on the MWCNTs by the flash light irradiation method.[39] The shift in the 2θ value of the peaks

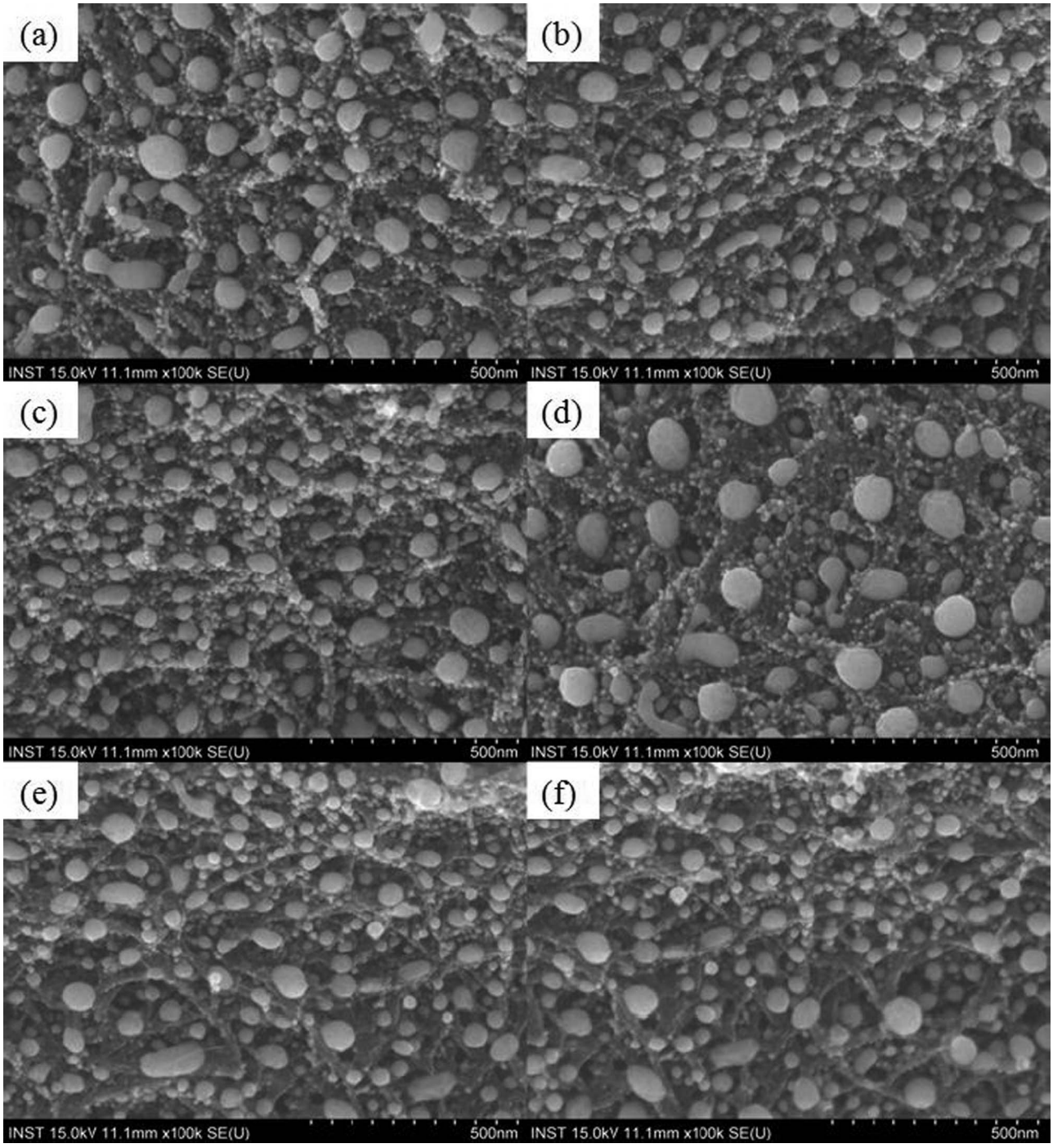

Figure 4. SEM images of (a) Pt_{100}/MWCNTs, (b) Pt_{50}-Ru_{50}/MWCNTs (c) Pt_{43}-Ru_{43}-Mo_{14}/MWCNTs, (d) Pt_{50}-$Ru_{37.5}$-$Mo_{12.5}$/MWCNTs, (e) Pt_{50}-Ru_{25}-Mo_{25} /MWCNTs, (f) Pt_{50}-$Ru_{12.5}$- $Mo_{37.5}$ /MWCNTs after flash irradiation with 60 J/cm^2.

corresponds to a decrease in the lattice parameter when compared to that of pure platinum due to the incorporation of ruthenium and molybdenum atoms.[40] Based on the (111) peaks of the Pt-based alloy catalysts, the mean size of the alloy particles was calculated according to Scherrer's formula, which may be expressed as:[41]

$$L = (0.9 \times \lambda)/(B \times \cos\theta) \quad [2.4]$$

where L is the mean size of the alloy particles, λ is the X-ray wavelength (CuKα $\lambda = 0.1541$ nm), θ is the maximum angle of the (111) peaks, and B is the full width at half-maximum of the (111) peak in radians. The mean sizes of the alloy particles were calculated as 12.63 nm for Pt_{100}/MWCNT, 10.42 nm for Pt_{50}-Ru_{50}/MWCNT, 7.44 nm for Pt_{43}-Ru_{43}-Mo_{14} /MWCNT, 8.31 nm for Pt_{50}-$Ru_{37.5}$-$Mo_{12.5}$ /MWCNT, 10.84 nm for Pt_{50}-Ru_{25}-Mo_{25}/MWCNT, and 12.66 nm for Pt_{50}-$Ru_{12.5}$-$Mo_{37.5}$/MWCNT. It is evident that the average particle sizes of the Pt-based alloy catalysts are almost the same regardless of the Pt, Ru, and Mo concentration. Such consistency is advantageous in the production of metal alloy catalysts, as the size and composition of the metal alloy nanoparticles can be controlled separately with little difficulty.

CV studies were conducted to evaluate the electro-catalytic activities of the Pt-based alloy catalysts for methanol oxidation in 0.5 M H_2SO_4 + 1.0 M CH_3OH. A scan rate of 50 mV/s and a potential range from −0.3 V to 1.0 V (vs. Ag/AgCl) were employed in the testing

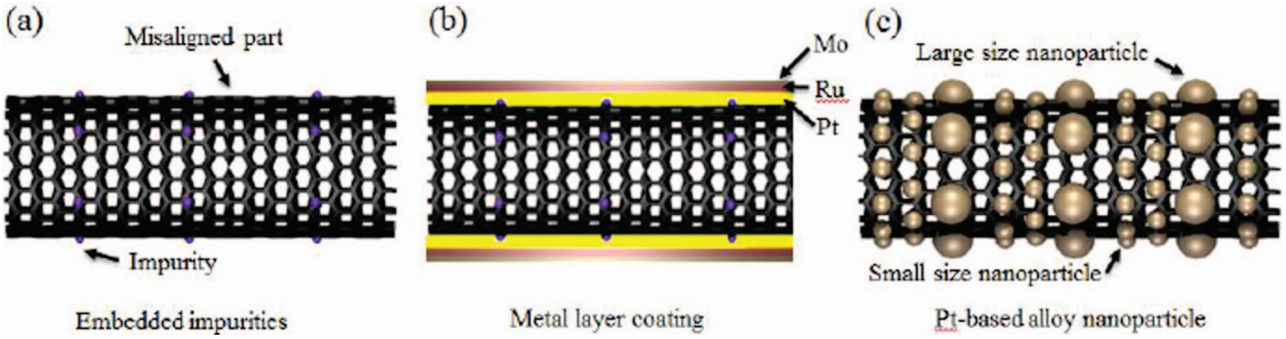

Figure 5. The schematics of the nanogranulation mechanism for MWCNT; (a) impurities are embedded, (b) metal layers are coated and (c) Pt-based alloys nanoparticles formed by flash light irradiation.

(Fig. 7). Two peaks corresponding to methanol oxidation and its intermediates were observed around 0.7 V and 0.5 V, respectively. As shown in Fig. 7, the CV features of the Pt-based alloy catalysts varied as a function of the Pt:Ru:Mo atomic ratio, indicating that methanol oxidation is related to the atomic ratio of Pt:Ru:Mo. Theoretically, methanol oxidation may proceed at 0.04 V with respect to a normal hydrogen electrode (NHE) via the following reaction:

$$CH_3OH + H_2O \rightarrow CO_2 + 6H^+ + 6e^- \quad [3]$$

As shown in Table I, the values of the onset potential of methanol oxidation for the different compositions were as follows: Pt_{100}/MWCNT (0.30 V vs. Ag/AgCl), Pt_{50}-Ru_{50}/MWCNT (0.28 V vs. Ag/AgCl), Pt_{43}-Ru_{43}-Mo_{14}/MWCNT (0.27 V vs. Ag/AgCl), Pt_{50}-$Ru_{37.5}$-$Mo_{12.5}$/MWCNT (0.28 V vs. Ag/AgCl), Pt_{50}-Ru_{25}-Mo_{25}/MWCNT (0.29 V vs. Ag/AgCl), and Pt_{50}-$Ru_{12.5}$-$Mo_{37.5}$/MWCNT (0.29 V vs. Ag/AgCl). The lower onset potentials of the Pt-based alloy catalysts (Cases 2 ~ 6) when compared to that of the pure Pt catalyst (Case 1) is clear evidence of the superior electrocatalytic activity of Pt-based alloy catalysts for methanol oxidation.

Another measurement that can be used to evaluate the methanol electro-oxidation activity of a catalyst is the ratio of the forward anodic peak current (I_f) to the backward anodic peak current (I_b). After 20 cycles, the reactions for all catalysts were fully activated and I_f, I_b were measured; the ratio of I_f/I_b was subsequently calculated. It has generally been known that CO poisoning increases I_b, which in turn decreases the I_f/I_b ratio.[19,42,43] Therefore, a high value of I_f/I_b implies relatively complete oxidation of methanol to carbon dioxide. In this work, the Pt_{100}/MWCNT catalyst exhibited the highest electrochemical reaction when compared to the other structures (Fig. 7). However, the intensity of the forward peak for the Pt_{100}/MWCNT catalyst was almost identical to that of the backward peak at both the 20th and 50th cycles, leading to I_f/I_b ratios of 1.12 and 1.14, respectively (Table I). In the Pt-based alloy catalysts, all of the forward peaks were higher than those of backward peaks. The number of methanol oxidation reactions at the 50th cycle increased when compared to that at the 20th cycle, while the amount of intermediate carbonaceous species gradually increased after the 20th cycle until the 50th cycle was reached. As a result, the I_f/I_b ratio was totally degraded between the 20th and 50th cycles, and then stabilized after 50 cycles in all cases (Table I).

To investigate the cycling capability of the Pt-based alloy catalysts, I_f/I_b was plotted with respect to the number of cycles for the Pt-based alloy catalysts (Fig. 8). As shown in Fig. 8 and Table I, the Pt_{43}-Ru_{43}-Mo_{14}/MWCNT catalyst had the highest I_f/I_b value among all catalysts evaluated in this study, regardless of the cycle number. In addition, the Pt_{43}-Ru_{43}-Mo_{14}/MWCNT catalyst maintained the highest value of I_f/I_b (2.81) when compared to the other Pt-based alloy catalysts after the 50th cycle.

From the above results, we concluded that the Pt_{43}-Ru_{43}-Mo_{14}/MWCNT catalyst prepared by flash light irradiation had the lowest onset potential, the lowest forward potential, and the highest I_f/I_b ratio of all catalysts.

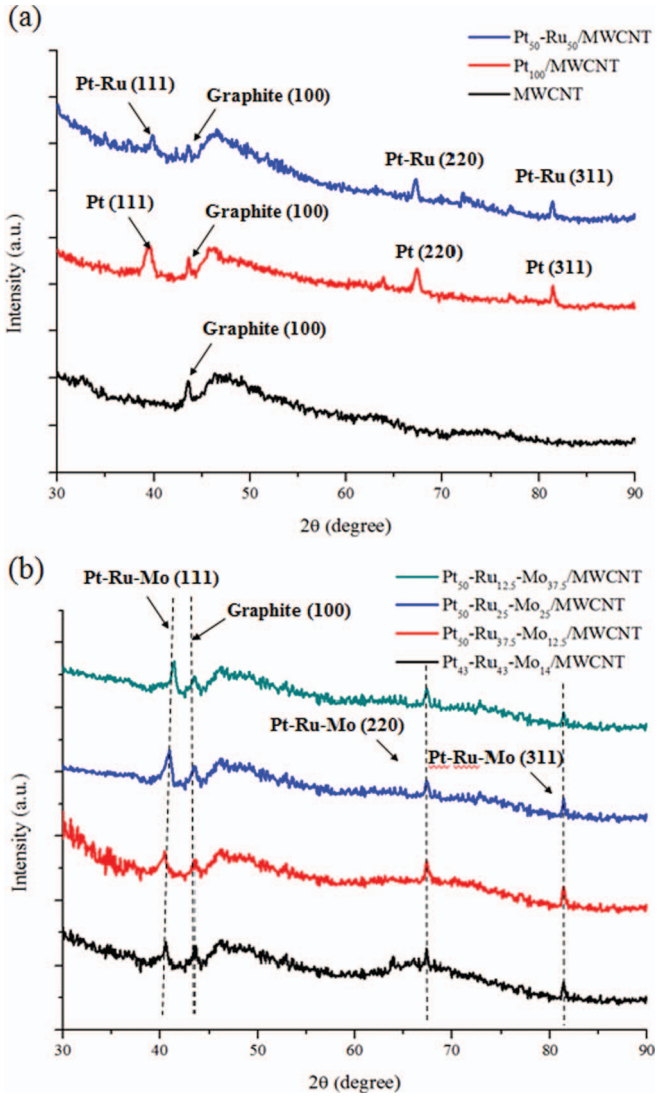

Figure 6. The XRD patterns of (a) MWCNTs (irradiated by flash light), Pt_{100}/MWCNTs, Pt_{50}-Ru_{50}/MWCNTs and (b) Pt_{43}-Ru_{43}-Mo_{14}/MWCNTs, Pt_{50}-$Ru_{37.5}$-$Mo_{12.5}$/MWCNTs, Pt_{50}-Ru_{25}-Mo_{25} /MWCNTs, Pt_{50}-$Ru_{12.5}$-$Mo_{37.5}$/MWCNTs.

Computational results.— DFT-GGA calculations were used to determine the equilibrium bond distance and adsorption energies of CO and OH absorbed on the (111) surface of a Pt-based alloy (Figs. 2 and 3); the computed values are listed in Tables II and III,

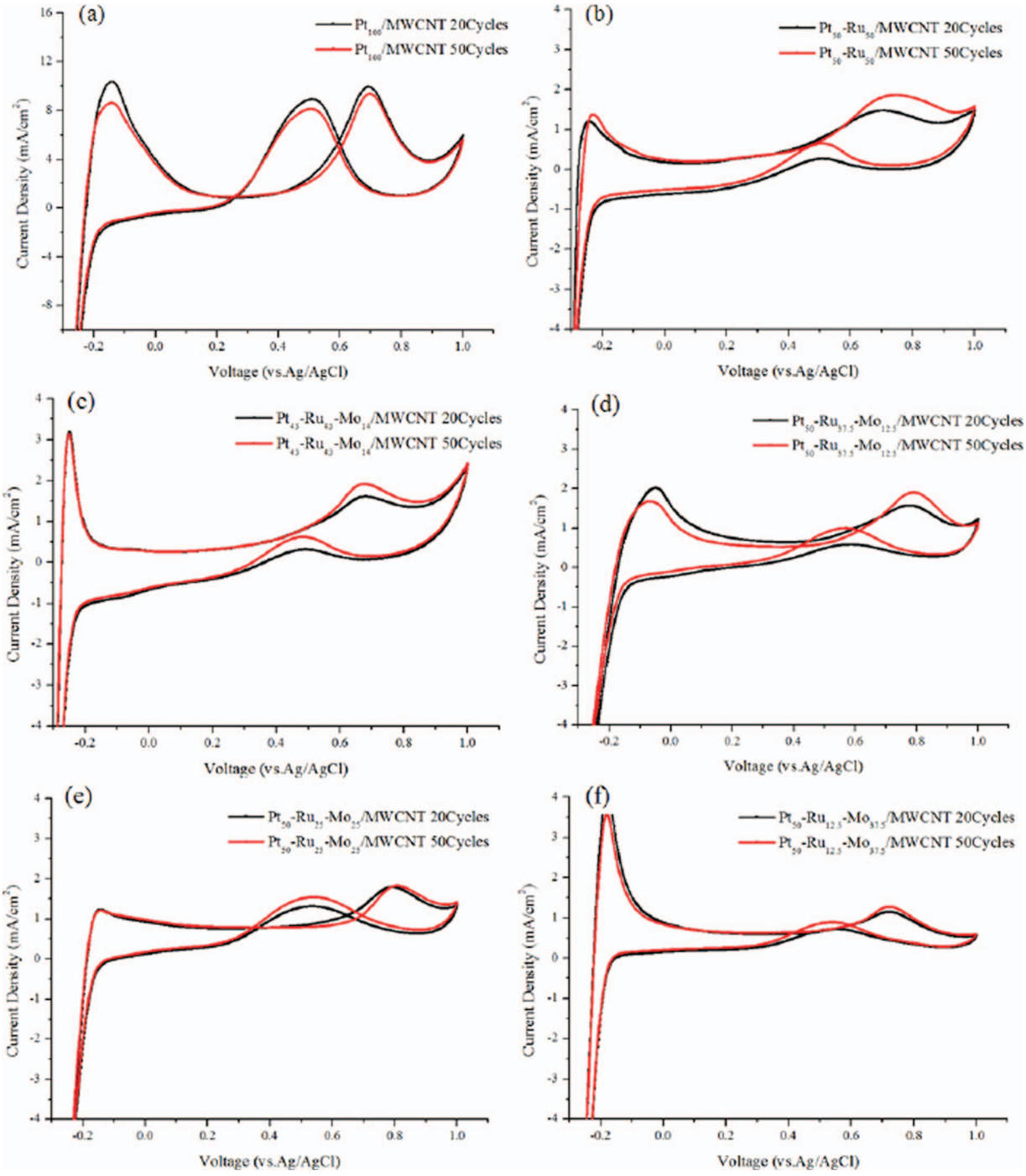

Figure 7. Cyclic voltammetry results for (a) Pt_{100}/MWCNTs, (b) Pt_{50}-Ru_{50}/MWCNTs (c) Pt_{43}-Ru_{43}-Mo_{14} /MWCNTs, (d) Pt_{50}-$Ru_{37.5}$-$Mo_{12.5}$/MWCNTs, (e) Pt_{50}-Ru_{25}-Mo_{25}/MWCNTs, (f) Pt_{50}-$Ru_{12.5}$-$Mo_{37.5}$ /MWCNTs measured in 0.5 M H_2SO_4 + 1 M CH_3OH at a scan rate of 50 mV/s.

Table I. Onset potential, peak potential and I_f/I_b ratios of the synthesized electrocatalysts.

Case	Catalyst	Onset potential (*V* vs. Ag/AgCl)	Forward potential (*V* vs. Ag/AgCl)	I_f/I_b after 20 cycles	Stabilized I_f/I_b
1	Pt_{100}	0.30 (±0.03)	0.705 (±0.04)	1.12 (±0.01)	1.14 (±0.01)
2	$Pt_{50}Ru_{50}$	0.28 (±0.02)	0.695 (±0.05)	5.13 (±0.12)	2.43 (±0.11)
3	$Pt_{43}Ru_{43}Mo_{14}$	0.27 (±0.02)	0.675 (±0.02)	5.40 (±0.05)	2.81 (±0.08)
4	$Pt_{50}Ru_{37.5}Mo_{12.5}$	0.28 (±0.03)	0.680 (±0.03)	2.70 (±0.07)	1.91 (±0.07)
5	$Pt_{50}Ru_{25}Mo_{25}$	0.29 (±0.02)	0.680 (±0.03)	2.11 (±0.06)	1.53 (±0.05)
6	$Pt_{50}Ru_{12.5}Mo_{37.5}$	0.29 (±0.02)	0.685 (±0.03)	1.57 (±0.02)	1.43 (±0.02)

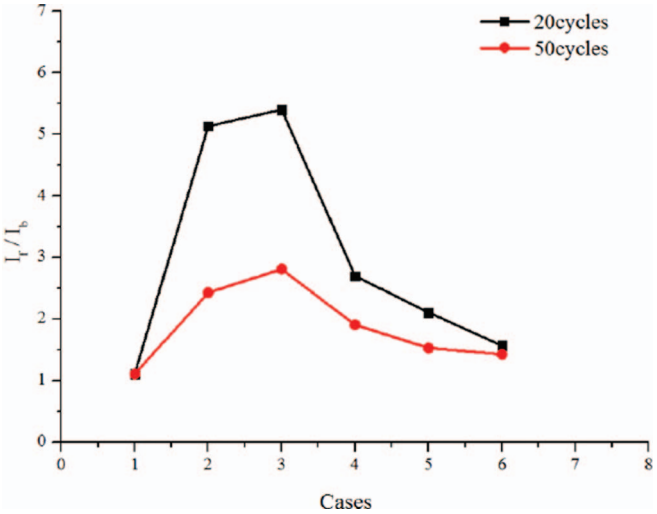

Figure 8. (a) Variation in the ratio of the forward anodic peak current to the backward anodic peak current (I_f/I_b) according to Pt-based alloy catalyst cases; Pt_{100}/MWCNTs (case 1), Pt_{50}-Ru_{50}/MWCNTs (case 2), Pt_{43}-Ru_{43}-Mo_{14} /MWCNTs (case 3), Pt_{50}-$Ru_{37.5}$-$Mo_{12.5}$/MWCNTs (case 4), Pt_{50}-Ru_{25}-Mo_{25}/MWCNTs (case 5) (f) Pt_{50}-$Ru_{12.5}$-$Mo_{37.5}$ /MWCNTs (case 6).

respectively. While many analytical results have been reported for CO and OH chemisorption on Pt-based alloys, there are no site-selective values available for both CO and OH chemisorption on Pt-Ru-Mo (111) alloy surfaces. This is because a DFT-GGA analysis for Pt-Ru-Mo ternary alloys has not yet been conducted, while Pt-based binary alloys have been examined in several works.[32–34] In the existing body of literature pertaining to the DFT-GGA analysis of Pt-based binary alloys, Ji and Koper et al. reported results obtained for Pt-Mo and Pt-Ru alloys.[34,35] However, it is difficult to directly compare such data with our findings because the boundary conditions and atomic ratio of the Pt-Ru alloys in both analyzes are different.[32–38] Nevertheless, the adsorption energy and the equilibrium bond distances of Ru and Mo in the Pt-based alloy were calculated at atop site with respect to the composition of the metal alloys. First, the adsorption energy of CO for the (111) Pt-based alloy was calculated. As shown in Table II, Pt_{100} (111) does indeed have the lowest CO adsorption energy while the Pt-Ru alloy case has higher CO adsorption energy than that of pure Pt case. The reason for the higher CO adsorption energy on the binary Pt-Ru alloy (Case 2) is attributed to the charge transfer effect for the bulk alloy; slight charge transfer, about 0.2 electron/atom, from Ru to Pt.[32] Therefore, the losing electronic charge from Ru can enhance the ability of Ru to accept charge from CO: reducing the repulsive interaction between the CO 5σ orbital and the metal d states. In contrast, accumulating charge on Pt atoms will have the opposite effect: an increase in repulsive interaction between the CO 5σ orbital and the metal d states.[32] Accordingly, the addition of Ru could lead to a stochastic increase in CO adsorption on the Pt-Ru binary alloy. Meanwhile, the

Table II. Adsorption energies of CO and OH on Pt-based alloy (111) with various compositions of catalysts.

Case	Catalyst	CO adsorption energy (eV)	OH adsorption energy (eV)
1	Pt_{100}	−1.57	−2.55
2	$Pt_{50}Ru_{50}$	−1.85	−3.04
3	$Pt_{43}Ru_{43}Mo_{14}$	−1.98	−3.30
4	$Pt_{50}Ru_{37.5}Mo_{12.5}$	−1.82	−3.22
5	$Pt_{50}Ru_{25}Mo_{25}$	−1.76	−3.15
6	$Pt_{50}Ru_{12.5}Mo_{37.5}$	−1.74	−3.11

Table III. Calculated structural parameters for optimized CO and OH adsorption cases, all distances are directly measured between two atoms.

		Pt-CO case		Pt-OH case		
Case	Catalyst	Pt-C (Å)	C-O (Å)	Pt-O (Å)	O-H (Å)	Pt-O-H (°)
1	Pt_{100}	1.88	1.16	2.01	0.99	105.93
2	$Pt_{50}Ru_{50}$	1.89	1.16	2.04	0.98	106.74
3	$Pt_{43}Ru_{43}Mo_{14}$	1.90	1.16	2.07	0.99	106.93
4	$Pt_{50}Ru_{37.5}Mo_{12.5}$	1.89	1.16	2.06	0.98	105.16
5	$Pt_{50}Ru_{25}Mo_{25}$	1.91	1.16	2.06	0.97	106.88
6	$Pt_{50}Ru_{12.5}Mo_{37.5}$	1.92	1.16	2.04	0.99	104.26

*Pt-C (Å): 1.86, C-O (Å): 1.15,[30] Pt-O (Å): 1.99, O-H (Å): 0.99, Pt-O-H (°): 107[30,31]

		Ru-CO case		Ru-OH case		
Case	Catalyst	Ru-C (Å)	C-O (Å)	Ru-O (Å)	O-H (Å)	Ru-O-H (°)
1	Pt_{100}					
2	$Pt_{50}Ru_{50}$	1.84	1.17	1.88	1.01	112.27
3	$Pt_{43}Ru_{43}Mo_{14}$	1.85	1.18	1.91	1.00	112.23
4	$Pt_{50}Ru_{37.5}Mo_{12.5}$	1.85	1.16	1.92	0.99	112.03
5	$Pt_{50}Ru_{25}Mo_{25}$	1.86	1.17	1.88	1.01	114.43
6	$Pt_{50}Ru_{12.5}Mo_{37.5}$	1.87	1.18	1.93	1.02	110.51

*Ru-C (Å): 1.85, C-O (Å): 1.16,[32] Ru-O (Å): 1.94, O-H (Å): 0.99, Ru-O-H (°): 112[33,34]

		Mo-CO case		Mo-OH case		
Case	Catalyst	Mo-C (Å)	C-O (Å)	Mo-O (Å)	O-H (Å)	Mo-O-H (°)
1	Pt_{100}					
2	$Pt_{50}Ru_{50}$					
3	$Pt_{43}Ru_{43}Mo_{14}$	2.02	1.17	1.83	1.01	118.04
4	$Pt_{50}Ru_{37.5}Mo_{12.5}$	2.02	1.16	1.85	0.99	117.07
5	$Pt_{50}Ru_{25}Mo_{25}$	2.03	1.17	1.86	1.00	117.81
6	$Pt_{50}Ru_{12.5}Mo_{37.5}$	2.04	1.17	1.88	1.01	117.16

*Mo-C (Å): 2.06, C-O (Å): 1.18,[35,36] Mo-O (Å): 1.86, O-H (Å): 0.99, Pt-O-H (°): 117[37]

CO adsorption energies for the Pt-Ru-Mo trimetallic compositions (Cases 4 ~ 6) except case 3 were lower than that calculated for the binary case (Table II). This may be due to the fact that the CO adsorption energy for pure Mo is lower than that for the other metals used in Pt-based binary alloys, with the exception of W, Re, and Zr.[36,37] Also, as the other reason, the smaller valence electron population of Mo atom is less favorable for the CO adsorption in spite of the electron transfers from the Mo atom to the Pt and Ru.[36] Thus, the lowest CO adsorption energy among all of the trimetallic alloys was observed for Case 6 with the highest Mo atomic ratio ($Pt_{50}Ru_{12.5}Mo_{37.5}$). It is noteworthy that the $Pt_{43}Ru_{43}Mo_{14}$ composition (Case 3) has the highest CO adsorption energy. This may be because the smaller atomic ratio of Pt and Mo in $Pt_{43}Ru_{43}Mo_{14}$ (Case 3) would induce a higher CO adsorption energy compared to any other cases.

To calculate the affinity for OH, the OH adsorption energies were calculated; the results are shown in Table II. The Pt_{100} (111) case shows the lowest adsorption energy for OH. In addition, the OH adsorption energy increased as the concentration of Ru and Mo were increased (Cases 2 ~ 6). Such a finding is reasonable, as it is widely known that Ru and Mo can easily absorb OH molecules from water at a low electrochemical potential of about 0.2 ~ 0.3 V vs. RHE.[3] In particular, the Pt_{43}-Ru_{43}-Mo_{14} composition (Case 3) shows the highest OH adsorption energy due to the low electrochemical potential of Ru and Mo (Table II).

The equilibrium bond distances of the (111) Pt-based alloy were also investigated so as to verify the suitability of our computational analysis. The equilibrium bond distances of Pt-C (1.88 Å) and C≡O (1.16 Å) on the (111) Pt-based alloy were in good agreement with the results obtained by Lynch et al (Pt-C distance = 1.86 Å, C≡O distance = 1.15 Å), as shown in Table II.[30] In addition, the equilibrium bond distances of Pt-O (about 2.04 Å), O-H (0.99 Å), and Pt-O-H (106.0°) on the (111) Pt-based alloy were quite similar to the values reported by Lynch and Michaelides et al. (see Fig. 3 and Table III).[30,31]

The equilibrium bond distances of Ru and Mo were also calculated in this work. As the results of CO chemisorptions, the equilibrium bond distances of Ru-C (1.84 ~ 1.87 Å) and C≡O (1.16 ~ 1.18 Å) on the (111) Pt-based alloy were similar with the reported value in Ge et al (Ru-C distance = 1.85 Å, C≡O distance = 1.16 Å) as shown in Table III.[32] Meanwhile, the C-metal bonding distance of Ru-CO case were decreased as the atomic ratio of Ru increased because the alloying with Pt strengthens the Ru-CO bond which induced the short bonding distance of Ru-C.[32] In the same manner, the equilibrium bond distances of Mo-C (2.02 ~ 2.04 Å) and C≡O (1.16 ~ 1.17 Å) on the (111) Pt-based alloy agreed well with those observed results in Ji and Tsuda et al (Mo-C distance = 2.06 Å, C≡O distance = 1.18 Å).[35,36] However, the C-metal bonding distance of Mo-CO case were longer than Pt and Ru cases because the CO bond is less strongly on Pt-Mo alloy than on pure Pt and Pt-Ru alloy.[35,36] Therefore, the Mo-C distances of Mo-CO case were increased as the atomic ratio of Mo increased as shown in Table III.

In the OH chemisorptions results, it was found that the bond distances for Ru-O (1.88 ~ 1.92 Å) and Mo-O (1.83 ~ 1.88 Å) were smaller than those of Pt-O (2.01 ~ 2.07 Å). Such a result is acceptable because the binding energy in the alloys of this study is inversely proportional to the M-O (M = Metal) bond distance (Table III). This trend is consistent with that observed in the previous research.[29–34] In particular, the bond distance for Mo-O in Pt_{43}-Ru_{43}-Mo_{14} is shorter than that in any other case, while the largest bond distance was calculated for Pt-O.

Finally, the molecular dynamics results were compared to the CV data obtained in 0.5 M H_2SO_4 + 1.0 M CH_3OH (Fig. 8). In the molecular dynamics simulations, pure Pt was found to have the lowest CO adsorption energy and OH adsorption energy, which is in good agreement with the CV test results (the most severe CO poisoning and lowest I_f/I_b value after 50 cycles were also observed for pure Pt). For the simulations of the trimetallic compositions, a higher CO adsorption energy and OH adsorption energy were obtained when compared to those in the binary and pure Pt cases. These results led to higher production of M(OH)ads than those of pure Pt and binary cases and removed the Pt(CO)ads species. Similar to the MD results, the trimetallic composition (Case 3) shows the best CO poisoning performance (highest I_f/I_b value of 2.81 among all cases after 50 cycles) in the CV tests (Table I). However, it was found that the electrochemical performance, i.e., the CO poisoning capability (I_f/I_b value), gradually decreased as the atomic ratio of Mo increased (Fig. 8). In addition, the trimetallic catalysts except the $Pt_{43}Ru_{43}Mo_{14}$ case which has the smaller atomic ratio of Pt (Cases 4, 5 and 6) show lower CO poisoning performance than that for the bimetallic case (Case 2). This may be due to the strong oxophilicity of Mo, which could lead to the surface segregation of Mo during alloy formation when the Mo ratio is high.[37] The segregation of a high atomic ratio of Mo might be the reason why electrochemical performance degradation, which could not be predicted in the MD simulations, occurs in Cases 4, 5 and 6. Meanwhile, the $Pt_{43}Ru_{43}Mo_{14}$ case (Case 6) which has the smaller atomic ratio of Pt and Mo leads the higher CO adsorption energy and the higher methanol oxidation performance as represented in above CO adsorption energy even though it is trimetallic catalyst which has 14% of atomic ratio of Mo. It is noteworthy that the Pt_{43}-Ru_{43}-Mo_{14} composition (Case 3) shows the best performance in both the CV tests and the molecular dynamics analysis. It could be concluded that the high performance of the Pt_{43}-Ru_{43}-Mo_{14} catalyst (Case 3) comes from the fact that well-formed alloy nanoparticle surfaces can easily react with OH species, while CO species cannot be effectively adsorbed on the alloy surfaces due to the low electrochemical potential of Mo and Ru on CO. These two phenomena would make the reaction in Equation 1.3 occur spontaneously, which could prevent the CO poisoning phenomenon.

Conclusions

In this work, we fabricated Pt-based alloy catalysts with various metal (Pt, Ru and Mo) concentrations via the flash light irradiation technique. Molecular dynamics simulations were also conducted using DFT-GGA calculations. It was found that the Pt_{43}-Ru_{43}-Mo_{14} alloy exhibits the best electro-chemical performance (i.e., highest I_f/I_b value) in both CV tests and the molecular dynamics analysis. The high I_f/I_b obtained with this composition is due to the elimination of CO poisoning phenomenon which is attributed to the removal of Pt(CO)ads and the production of Ru(OH)ads and Mo(OH)ads rather than Pt(OH)ads by alloying the Ru and Mo.

Acknowledgment

This work was supported by a National Research Foundation of Korea (NRF) funded by the Ministry of Education (Nos. 2010-0007120, 2012R1A6A1029029 and 2013M2A2A9043280). This research was also supported by a grant from the Technology Development Program for Strategic Core Materials funded by the Ministry of Trade, Industry & Energy, Republic of Korea (Project No. 10047758). Also, this work was supported by the Chungcheong institute for regional program evaluation promotion projects of the Korean Ministry of Knowledge Economy (No. A002200085).

References

1. A Hamnett, *Catalysis Today.*, **38**, 445 (1997).
2. J. Kua and W. A. Goddard, *J. Am. Chem. Soc .*, **121**, 10928 (1999).
3. H. Liu, D. Xia, and J. Zhang, *Platinum-based Alloy Catalysts for PEM Fuel Cells.*, p. 631, Springer, London (2008).
4. J. T. Muller, P. M. Urbran, W. F. Holderich, K. M. Colbow, J. Zhang, and D. P. Wilkinson, *J. Electrochem. Soc.*, **147**, 4058 (2000).
5. M. K. Min, J. Cho, K. Cho, and H. Kim, *Electrochimica Acta.*, **45**, 4211 (2000).
6. A. S. Arico, P. Creti, H. Kim, R. Mantegna, N. Giordano, and V Antonucci, *J. Electrochem. Soc.*, **143**, 3950 (1996).
7. H. Liu, C. Song, L. Zhang, J. Zhang, H. Wang, and D. P. Wilkinson, *J. Power Sources.*, **155**, 95 (2006).
8. J. H. Choi, K. W. Park, B. K. Kwon, and Y. E. Sung, *J. Electrochem. Soc.*, **150**, A973 (2003).

9. T. Huang, T. J. Liu, R. Li, W. Cai, and A. Yu, *Electrochem. Comm un.*, **11**, 643 (2009).
10. S. Pasupathi and V. Tricoli, *J. Solid State Electr.*, **12**, 1093 (2008).
11. K. L. Ley, R. Liu, C. Pu, Q. Fan, N. Leyarovska, C. Segre, and E. S. Smotkin, *J. Electrochem. Soc.*, **144**, 1543 (1997).
12. A. F. Shao, Z. B. Wang, Y. Y. Chu, Z. Z. Jiang, G. P. Yin, and Y. Liu, *Fuel Cells.*, **10**, 472 (2010).
13. S. A. Lee, K. W. Park, J. H. Choi, B. K. Kwon, and Y. E. Sung, *J. Electrochem. Soc.*, **149**, A1299 (2002).
14. K. Ding, H. Yang, Y. Cao, C. Zheng, S. B. Rapole, and Z. Guo, *Mater. Chem. Phys.*, **142**, 403 (2013).
15. K. Ding, Y. Wang, H. Yang, C. Zheng, Y. Cao, H. Wei, Y. Wang, and Z. Guo, *Electrochim. Acta*, **100**, 147 (2013).
16. K. Ding, H. Jia, S. Wei, and Z. Guo, *Ind. Eng. Chem. Res.*, **50**, 7077 (2011).
17. K. Ding, G. Yang, S. Wei, P. Mavinakuli, and Z. Guo, *Ind. Eng. Chem. Res.*, **49**, 11415 (2010).
18. Y. W. Song, S. H. Park, W. S. Han, J. M. Hong, and H. S. Kim, *Mater. Lett.*, **65**, 2510 (2011).
19. S. H. Park, H. M. Jung, Sukkee Um, Y. W. Song, and H. S. Kim, *Int. J. of Hydrogen Energ.*, **37**, 12597 (2012).
20. N. Tsiouvaras, M. V. Martínez-Huerta, O. Paschos, U. Stimming, J. L. G. Fierro, and M. A. Peña, *Int. J. Hydrogen Energ.*, **35**, 11478 (2010).
21. C. Lamy, A. Lima, V. LeRhun, F. Delime, C. Coutanceau, and J. M. Léger, *J. Power Sources.*, **105**, 283 (2002).
22. A. Lima, A. C. Coutanceau, J. M. LÉger, and C. Lamy, *J. Appl. Electrochem.*, **31**, 379 (2001).
23. D. A. Stevens, J. M. Rouleau, R. E. Mar, R. T. Atanasoski, A. K. Schmoeckel, M. K. Debe, and J. R. Dahn, *J. Electro chem. Soc.*, **154**, B1211 (2007).
24. M. D. Segall, P. J. D. Lindan, M. J. Probert, C. J. Pickard, P. J. Hasnip, S. J. Clark, and M. C. Payne, *J. phys-condens. mat.*, **14**, 2717 (2002).
25. Z. Yang, Z. R. Wu, and J. A. Rodriguez, *Phys . Rev . B.*, **65**, 155409 (2002).
26. J. A. Rodriguez, J. M. Ricart, A. Clotet, and F. Illas, *J. Chem. Phys.*, **115**, 454 (2001).
27. D. Vanderbilt, *Phys. Rev. B*, **41**, 7892 (1990).
28. H. J. Monkhorst and J. D. Pack, *Phys. Rev. B*, **13**, 5188 (1976).
29. Z. Jiang, L. Li, J. Xu, and T. Fang, *Appl. Surf. Sci.*, **286**, 115 (2013).
30. M. Lynch and P. Hu, *Surf. Sci.*, **458**, 1 (2000).
31. A. Michaelides and P. Hu, *J. Chem. Phys.*, **114**, 513 (2001).
32. Q. Ge, S. Desai, M. Neurock, and K. Kourtakis, *J. Phys. Chem. B*, **105**, 9533 (2001).
33. B. C. Han and G. Ceder, *Phys. Rev. B*, **74**, 205418 (2006).
34. M. T. M. Koper, T. E. Shubina, and R. A. van Santen, *J. Phys. Chem . B*, **106**, 686 (2002).
35. Z. Ji and J. Q. Li, *Chem. Phys. Lett*, **424**, 111 (2006).
36. M. Tsuda and H. Kasai, *Phys. Rev. B*, **73**, 155405 (2006).
37. Y. Ishikawa, M. S. Liao, and C. R. Cabrera, *Surf. Sci.*, **513**, 98 (2002).
38. T. E. Shubina and M. T. M. Koper, *Electrochimica Acta.*, **47**, 3621 (2002).
39. X. Zhang, F. Zhang, and K. Y. Chan, *J. Mater. Sci.*, **39**, 5845 (2004).
40. S. Mukerjee and R. C. Urian, *Electrochimica Acta.*, **47**, 3219 (2002).
41. W. Li, C. Liang, W. Zhou, J. Qju, Z. Zhou, G. Sun, and Q. Xin, *J. Phys. Chem. B*, **107**, 6292 (2003).
42. Y. Lin, X. Cui, C. H. Yen, and C. M. Wai, *Langmuir.*, **21**, 11474 (2005).
43. C. T. Hsieh, J. Y. Lin, and S. Y. Yang, *Physica E.*, **41**, 373 (2009).